INTERNATIONAL JOURNAL FOR NUMERICAL METHODS IN FLUIDS
Int. J. Numer. Meth. Fluids 2009; **60**:203–225
Published online 9 September 2008 in Wiley InterScience (www.interscience.wiley.com). DOI: 10.1002/fld.1885

Mobility-dependent bifurcations in capillarity-driven two-phase fluid systems by using a lattice Boltzmann phase-field model

J. J. Huang, C. Shu*,† and Y. T. Chew

Department of Mechanical Engineering, National University of Singapore, 10 Kent Ridge Crescent, Singapore 119260, Singapore

SUMMARY

Bifurcations in capillarity-driven two-phase fluid systems, due to different mobilities in phase-field models for such systems, are studied by using a lattice Boltzmann method (LBM). Specifically, two-dimensional (2D) and three-dimensional (3D) droplets on a flat wall with given wettability variations are investigated. It is found that the mobility controls the rate of diffusive relaxation of the phase field from non-equilibrium toward equilibrium, and similar to previous findings on mechanically driven two-phase systems, the mobility is closely related to the contact line velocity. For the cases investigated, different mobilities across a critical value result in fundamentally different system evolution routes and final stable equilibrium states. These results may provide some implications for phase-field study of droplet manipulations by surface wettability adjustments in microfluidics. Copyright © 2008 John Wiley & Sons, Ltd.

Received 5 March 2008; Revised 17 June 2008; Accepted 17 June 2008

KEY WORDS: droplet; mobility; contact line; bifurcation; lattice Boltzmann method

1. INTRODUCTION

The study of immiscible two-phase fluid systems has its significance in both theoretical and practical aspects but is still a challenging problem. There is much enriched physics such as phase separation and mixing in these systems, and they are commonly encountered in such industries as cosmetic, food and pharmacy. Modeling of these systems is usually difficult due to complex interfaces between different fluids, as well as those between the fluids and solid walls [1]. In the literature, the phase-field models (also known as diffuse interface models) have been shown to hold good prospects in studying the dynamics of such systems [2, 3]. In phase-field models for multicomponent fluid flows, the underlying governing equations are usually composed of

*Correspondence to: C. Shu, Department of Mechanical Engineering, National University of Singapore, 10 Kent Ridge Crescent, Singapore 119260, Singapore.
†E-mail: mpeshuc@nus.edu.sg

the Navier–Stokes equations, which are conservation laws for the mass and momentum, and the Cahn–Hilliard equation (CHE), which describes the evolution of the phase-field function. If the mobility is assumed to be constant, the CHE may be written as $\partial_t \phi + (\mathbf{u} \cdot \nabla)\phi = M\nabla^2 \mu$, with ϕ being the phase-field function (or concentration), $\mathbf{u}$ the fluid velocity, μ the chemical potential and M the mobility. This convection–diffusion equation is very similar to the pure advection equation (without the diffusion term) in some other methods for multiphase flows, such as the level set and volume of fluid (VOF) methods. In these methods, similar diffusion should also exist due to the smoothing procedure necessary for calculating the interfacial tension force. Diffusion might be completely eliminated only in pure interface tracking methods.As compared with level set and VOF methods, the explicit inclusion of the diffusion term in the CHE, with its magnitude proportional to M, provides a physical relaxation mechanism for the concentration. Such a mechanism leads to the flexibility of phase-field models to accommodate various singularities, for instance, the pressure jump across a curved interface and the stress singularity in contact line dynamics [3, 4].

Previously some researchers have given a few analyses on the mobility, both as a computational parameter related to asymptotics of numerical methods and as a physical one involving diffusional properties in mixing, coalescence and contact line problems. Jacqmin [3] found, by some theoretical analysis and numerical investigations, that the mobility should be bounded between $O(\varepsilon^2)$ and $O(\varepsilon)$ (ε being the dimensionless interface thickness) in order to carry out an appropriate diffuse interface simulation that approximates the sharp interface solutions. Jacqmin [4] provided a detailed analysis on the inner regions surrounding a three-phase contact line (point) and found a length scale (here denoted as l_{CL}) for such small regions determined by the dynamic viscosity and the mobility, $l_{\mathrm{CL}} \propto \sqrt{\eta M}$ (η being the dynamic viscosity). Chen *et al*. [5] similarly identified a length scale in the moving contact line problems for the dissipative relaxation of the concentration, which is related to the interfacial thickness, the concentration diffusivity and the boundary velocity. Kendon *et al*. [6] addressed the significance of using an appropriate mobility, similar to the conclusion reached in [3], in the lattice Boltzmann method (LBM) framework; they also addressed the difficulty in using a concentration-dependent mobility in LBM. Briant and Yeomans [7] studied the contact line dynamics using LBM and derived a length scale proportional to $M^{1/4}$ for the region in which the diffusive effects become significant and argued that their results match the classical work using a slip length model. Inamuro *et al*. [8] found, by using the LBM, that in bubble rising problems, the mobility affects the coalescence of two bubbles. Vladimirova and Mauri [9] and most recently Lamorgese and Mauri [10] showed some diffuse interface simulations of droplet coalescences when the system is suddenly changed from two- to one-phase region; results from both investigations illustrate that different mobilities (Peclet numbers in the original articles) may lead to qualitatively different mixing outcome. Khatavkar *et al.* [11] also discussed the scaling issues in diffuse interface models and pointed out that it is necessary to know how to adapt the mobility in accordance with the artificial enlargement of the interface thickness so as to capture the bulk flow phenomena. Zheng *et al*. [12] discovered that, similar to [8], large mobility expedites the merging processes of two close bubbles.

It has become obvious that the mobility is an important parameter in the study of multiple phase or fluid flows by the phase-field modeling. However, the effect of mobility in various flows may be diverse and it certainly deserves comprehensive investigations, either as a physical property or as a numerical parameter. The purpose of this paper is to study the interesting bifurcation phenomena due to different mobilities in systems with droplets driven by variations in surface wettability. Here the mobility is viewed as a physical parameter controlling diffusion in CHE. It is noted that some

DOI: 10.1002/fld

cases shown below might occur only at submicrometer or even smaller scales, which is necessary to allow the diffusion to become important enough to affect the flow significantly.

This paper is organized as follows. Section 2 introduces the free-energy-based diffuse interface model for two-phase fluids. Section 3 describes the lattice Boltzmann formulation and the wetting boundary conditions. In Section 4, simulation results and some discussions are presented for 2D and 3D droplets on a lyophobic wall and 3D droplets on chemically heterogeneous surfaces to illustrate the bifurcations occurring in these systems under different mobilities. Section 5 concludes this paper.

2. DIFFUSE INTERFACE MODEL FOR TWO-PHASE FLUID SYSTEMS

When a square gradient interfacial energy density is assumed, the free energy functional may be expressed as

$$F(\phi, \nabla\phi) = \int_V (\psi(\phi) + (\kappa/2)|\nabla\phi|^2)\,\mathrm{d}V \tag{1}$$

where ϕ is the concentration varying smoothly across the interfacial region, $\psi(\phi)$ is the bulk free energy density, $(\kappa/2)|\nabla\phi|^2$ is the interfacial energy density with κ being a constant and V denotes the fluid volume. Among various forms of bulk free energy density [12–14], the simplest one is the double well form, which is adopted in the present study and expressed as

$$\psi(\phi) = a(\phi+1)^2(\phi-1)^2 \tag{2}$$

where a is a constant (note: κ and a are related to the interfacial tension and interface thickness; detailed relations to be given later). Across a flat interface, ϕ changes from 1 to -1. The chemical potential μ is calculated by taking the variation of the free energy functional with respect to the concentration

$$\mu = \delta F/\delta\phi = \psi'(\phi) - \kappa\nabla^2\phi = 4a\phi(\phi^2-1) - \kappa\nabla^2\phi \tag{3}$$

For a flat interface, one can obtain the analytical solution of the interface profile

$$\phi(z) = \tanh(z/(W/2)) \tag{4}$$

where z is the coordinate perpendicular to the interface and W is the interface thickness given by

$$W = \sqrt{2\kappa/a} \tag{5}$$

Note that the definition of interface thickness may be different in different papers. Here from Equation (4), W corresponds to the distance across which ϕ varies from -0.76159 ($z=-W/2$) to 0.76159 ($z=W/2$).

The surface tension σ can be calculated as

$$\sigma = \kappa\int_{-\infty}^{\infty} (\mathrm{d}\phi/\mathrm{d}z)^2\,\mathrm{d}z = (4/3)\sqrt{2\kappa a} \tag{6}$$

Using Equations (5) and (6), one can express the coefficients a and κ in terms of σ and W as follows:

$$a = (3\sigma)/(4W) \tag{7a}$$

$$\kappa = 3\sigma W/8 \tag{7b}$$

DOI: 10.1002/fld

Similar to [4], for simplicity yet without losing the core physics, we consider only systems with a constant mobility and with no difference in density or viscosity. For such systems, the full governing equations can be expressed as

$$\nabla \cdot \mathbf{u} = 0 \tag{8a}$$

$$\partial_t \mathbf{u} + (\mathbf{u} \cdot \nabla)\mathbf{u} = -\nabla S_p + \nu \nabla^2 \mathbf{u} - \phi \nabla \mu \tag{8b}$$

$$\partial_t \phi + (\mathbf{u} \cdot \nabla)\phi = M \nabla^2 \mu \tag{8c}$$

where ν is the kinematic viscosity and S_p is used to enforce the incompressibility [4]. After non-dimensionalization with a characteristic density ρ_c, a characteristic length L_c, a characteristic velocity U_c and a characteristic time L_c/U_c, they become

$$\nabla \cdot \mathbf{u} = 0 \tag{9a}$$

$$\partial_t \mathbf{u} + (\mathbf{u} \cdot \nabla)\mathbf{u} = -\nabla S_p + Re^{-1} \nabla^2 \mathbf{u} - (Re\,Ca)^{-1} \phi \nabla \{Ch^{-1}[3\phi(\phi^2 - 1)] - Ch(3\nabla^2 \phi/8)\} \tag{9b}$$

$$\partial_t \phi + (\mathbf{u} \cdot \nabla)\phi = Pe^{-1} \nabla^2 \{Ch^{-1}[3\phi(\phi^2 - 1)] - Ch(3\nabla^2 \phi/8)\} \tag{9c}$$

where Re is the Reynolds number, $Re = U_c L_c/\nu$, which reflects the ratio of the inertial force to the viscous force, Ca is the capillary number, $Ca = \rho_c \nu U_c/\sigma$, which measures the ratio of the viscous force to the surface tension force. In addition, there appear two parameters that are defined uniquely in diffuse interface models. One is the Cahn number, $Ch = W/L_c$, which is the ratio of the interface thickness to the characteristic length, and the other is the Peclet number, $Pe = U_c L_c^2/M\sigma$, which reflects the ratio of the convection intensity to the diffusion one. It is noted that in [11], the Peclet number is defined differently as (in terms of the present symbols) $U_c L_c W/M\sigma$, which is related to the present one as $U_c L_c W/M\sigma = PeCh$. If that definition is adopted, then the right-hand side of Equation (9c) will become $Pe^{-1}\nabla^2[3\phi(\phi^2 - 1) - Ch^2(3\nabla^2\phi/8)]$. We have to indicate that sometimes it is difficult to identify the characteristic quantities before the simulation. For instance, for a chemically driven droplet it is almost impossible to know the characteristic (e.g. the maximum) velocity beforehand because the actual value is determined not only by the droplet size and the surface tension but also by the initial configuration and the wetting property (more generally, the gradient of the chemical potential), and even the mobility as shown later. Hence, we use the mobility instead of the Peclet number to differentiate the cases. Nevertheless, the corresponding dimensionless numbers can be calculated from the simulation results, and the Peclet numbers of most cases will be so small that the diffusion is important to determine the flow characteristics.

There have been many studies on the direct numerical solutions of the above set of equations. In this paper, we focus on another type of method—the LBM—which approximates them in the long-wavelength and long-time limit yet proves to be fairly efficient and easy to implement [15]. LBM is different from the direct solving methods at least in the following aspects: (i) LBM uses a set of distribution functions, the moments of which include more than the velocity, pressure and the concentration and simple collision-streaming loops are performed on each time step; (ii) the non-slip boundary condition is implemented indirectly through the bounce-back condition for the distribution functions and (iii) the wetting boundary condition is implemented through the equilibrium distribution functions and, in the present model, the collision step. The differences and comparisons between the two types of methods may deserve further research work, but they are out of the scope of this work. Furthermore, we restrict our focus within the free-energy-based LBM, which is closer to the original concept of diffuse interface models.

DOI: 10.1002/fld

3. LATTICE BOLTZMANN MODEL FOR IMMISCIBLE TWO-PHASE FLUIDS

3.1. The LBM formulation

In this subsection, we briefly outline the free-energy-based LBM for immiscible two-phase fluids. The free energy is almost identical to that defined in Equation (1) except that an additional term is inserted into the volume integration to enforce incompressibility [1, 6] and the surface energy contribution is included to model the wetting on solid walls [7, 16]:

$$F(\phi, \nabla\phi) = \int_V (\rho c_s^2 \ln\rho + \psi(\phi) + (\kappa/2)|\nabla\phi|^2)\,\mathrm{d}V + \int_S \varphi(\phi_S)\,\mathrm{d}S \tag{10}$$

More details about the surface energy and wetting boundary conditions are given in the next subsection.

The lattice Boltzmann equations are given as

$$f_i(\mathbf{x}+\mathbf{e}_i\delta_t, t+\delta_t) - f_i(\mathbf{x},t) = -(f_i(\mathbf{x},t) - f_i^{\mathrm{eq}}(\mathbf{x},t))/\tau_f + \delta_t w_i \mathbf{e}_{i\alpha}(\mu\partial_\alpha\phi)/c_s^2 \tag{11a}$$

$$g_i(\mathbf{x}+\mathbf{e}_i\delta_t, t+\delta_t) - g_i(\mathbf{x},t) = -(g_i(\mathbf{x},t) - g_i^{\mathrm{eq}}(\mathbf{x},t))/\tau_g \tag{11b}$$

where f_i are the distribution functions for the hydrodynamics fields (ρ, u_α, S_p), g_i are the distribution functions for the concentration field (ϕ), c_s is the 'sound speed', δ_t is the time step and w_i are the weights associated with the discrete velocities $\mathbf{e}_i$. Note that summation over repeated subscripts for spatial coordinates (i.e. the Greek letters) is assumed throughout the paper (not applicable for other subscripts). For the D2Q9 [7] and D3Q15 [6] models used here, the sound speed is related to the unit lattice speed as

$$c = \sqrt{3}c_s \tag{12}$$

The details about $\mathbf{e}_i$ and w_i can be easily found in the literature [6, 7] and will be omitted here for conciseness. In Equations (11a) and (11b), τ_f and τ_g are the relaxation parameters related to the fluid viscosity and the mobility, respectively; the equilibrium distribution functions, f_i^{eq} and g_i^{eq}, are calculated from the local density, velocity, concentration and the chemical potential as follows:

$$f_i^{\mathrm{eq}} = w_i\{A_i + \rho[e_{i\alpha}u_\alpha/c_s^2 + u_\alpha u_\beta(e_{i\alpha}e_{i\beta} - c_s^2\delta_{\alpha\beta})/(2c_s^4)]\} \tag{13a}$$

$$g_i^{\mathrm{eq}} = w_i(B_i + \phi e_{i\alpha}u_\alpha/c_s^2) \tag{13b}$$

with the coefficients A_i and B_i given by

$$A_i = \begin{cases} (\rho c_s^2 + \phi\mu)/c_s^2 = A & (i>0) \\ w_0^{-1}[\rho - (1-w_0)A] & (i=0) \end{cases} \tag{14a}$$

$$B_i = \begin{cases} \tilde{M}\mu/c_s^2 = B & (i>0) \\ w_0^{-1}[\phi - (1-w_0)B] & (i=0) \end{cases} \tag{14b}$$

DOI: 10.1002/fld

Here $\tilde{M}$ is a parameter related to the mobility M as $M=(\tau_g-1/2)\tilde{M}\delta_t$ and in the following simulations, $\tau_g=1$, $M=(1/2)\tilde{M}\delta_t$. The distribution functions satisfy the following relations:

$$\sum_i f_i=\sum_i f_i^{\mathrm{eq}}=\rho \tag{15a}$$

$$\sum_i g_i=\sum_i g_i^{\mathrm{eq}}=\phi \tag{15b}$$

$$\sum_i e_{i\alpha}f_i=\sum_i e_{i\alpha}f_i^{\mathrm{eq}}=\rho u_\alpha \tag{16a}$$

$$\sum_i e_{i\alpha}g_i=\sum_i e_{i\alpha}g_i^{\mathrm{eq}}=\phi u_\alpha \tag{16b}$$

$$\sum_i e_{i\alpha}e_{i\beta}f_i^{\mathrm{eq}}=\rho u_\alpha u_\beta+(\rho c_s^2+\phi\mu)\delta_{\alpha\beta} \tag{17a}$$

$$\sum_i e_{i\alpha}e_{i\beta}g_i^{\mathrm{eq}}=\tilde{M}\mu\delta_{\alpha\beta} \tag{17b}$$

When the Chapman–Enskog multiscale analysis [7] is applied to this model, the set of governing equations can be obtained in the long-time and long-wavelength limit. It is noted that the above LBM is close to that in [6]. However, the way to deal with the surface tension force has been modified, which results in much smaller spurious currents and better isotropy of the velocity field in the interfacial region. The main idea is to rewrite the momentum equation as

$$\partial_t\mathbf{u}+\nabla\cdot(\mathbf{uu}+(S_p+\phi\mu)\overleftrightarrow{I})=\nu\nabla^2\mathbf{u}+\mu\nabla\phi \tag{18}$$

where $\overleftrightarrow{I}$ denotes the unit tensor of the second order. As seen in Equations (11a), (13a) and (14a), the surface tension force is separated into two parts: one put into the equilibrium distribution functions and the other applied as a body force in the collision step. Such rearrangement and implementation originate from [12]. In dealing with the surface tension force by this way, the highest order of derivatives in the forcing term changes from the third $\nabla(\nabla^2)$, as seen in $\nabla\mu=\nabla[\psi'(\phi)-\kappa\nabla^2\phi]$, to the second ∇^2, as seen in $\mu=\psi'(\phi)-\kappa\nabla^2\phi$.

With the given appropriate initial conditions, the computation follows the standard LBM cycle:

(1) Collision:

$$f_i(\mathbf{x},t^+)=[1-(1/\tau_f)]f_i(\mathbf{x},t)+(1/\tau_f)f_i^{\mathrm{eq}}(\mathbf{x},t)+\delta_t w_i\mathbf{e}_{i\alpha}(\mu\partial_\alpha\phi)/c_s^2$$

$$g_i(\mathbf{x},t^+)=[1-(1/\tau_g)]g_i(\mathbf{x},t)+(1/\tau_g)g_i^{\mathrm{eq}}(\mathbf{x},t)$$

(2) Applying boundary conditions for f_i, g_i.

(3) Streaming:

$$f_i(\mathbf{x}+\mathbf{e}_i\delta_t,t+\delta_t)=f_i(\mathbf{x},t^+)$$

$$g_i(\mathbf{x}+\mathbf{e}_i\delta_t,t+\delta_t)=g_i(\mathbf{x},t^+)$$

DOI: 10.1002/fld

(4) Calculating the macroscopic variables: ρ, u_α, ϕ, $\partial_\alpha\phi$, μ and specifying $\partial_\alpha\phi$ on the solid boundaries.
(5) Calculating the equilibrium distribution functions: f_i^{eq} and g_i^{eq}.

3.2. *Boundary conditions*

In LBM, the bounce-back scheme is usually applied on a solid wall for the distribution functions. Figure 1 gives the illustration for the D2Q9 model on a lower wall (note that there are different versions of bounce back and the one illustrated here is the by-node scheme). Take the distribution functions f_i as an example (the same conditions are applied for g_i). After the streaming step, f_6, f_7 and f_8 are bounced back in their respective opposition directions. In the next time step, their values are given to f_2, f_3 and f_4, respectively.

Now we give some further discussions on the surface energy and the wetting boundary conditions. The surface energy $\varphi(\phi_S)$ in Equation (10) is assumed to be a simple linear function of the concentration on the wall [7, 16]

$$\varphi(\phi_S) = -\omega\phi_S \tag{19}$$

where ω is the parameter related to the surface wetting property characterized by the static contact angle (CA) θ. By minimizing the total free-energy functional, one can obtain a natural boundary condition for the concentration as

$$\kappa\mathbf{n}\cdot(\nabla\phi)_S = -\omega \tag{20}$$

where $\mathbf{n}$ is the local normal direction of the wall pointing into the fluid. The static CA θ (measured in the fluid with $\phi = 1$) can be shown to satisfy the following equation:

$$\cos\theta = (1/2)[(\sqrt{1+\tilde{\omega}})^3 - (\sqrt{1-\tilde{\omega}})^3] \tag{21}$$

with the dimensionless parameter $\tilde{\omega}$ given by

$$\tilde{\omega} = \omega/(\sqrt{2\kappa a}) \tag{22}$$

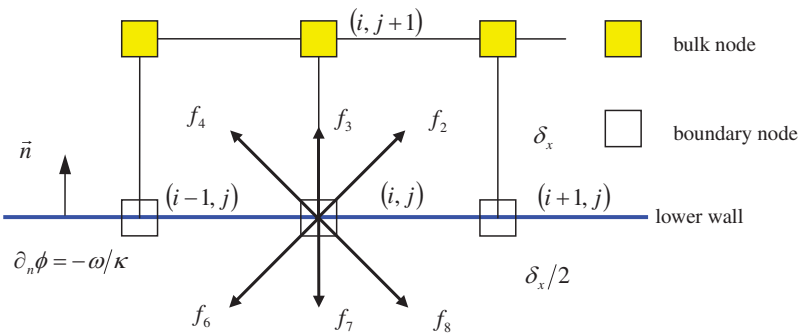

Figure 1. Illustration of the bounce-back scheme in LBM on the lower wall and the wetting boundary condition for the order parameter.

DOI: 10.1002/fld

In the implementation of the wetting boundary conditions (specifically, to enforce the natural boundary condition) the method given in [16] has been followed. From Equation (20), to apply the wetting condition is essentially to enforce a given normal gradient of the order parameter on the wall $(\partial_n \phi)_S = -\omega/\kappa$. For the boundary nodes shown in Figure 1, the following formulas are used to evaluate the derivatives:

$$\partial_x \phi|_{i,j} \approx (\phi_{i+1,j} - \phi_{i-1,j})/(2\delta_x) \tag{23}$$

$$\partial_y \phi|_{i,j} = -\omega/\kappa \tag{24}$$

$$\partial_{xx} \phi|_{i,j} \approx (\phi_{i+1,j} - 2\phi_{i,j} + \phi_{i-1,j})/\delta_x^2 \tag{25}$$

$$\partial_{yy} \phi|_{i,j} \approx (6\omega\delta_x/\kappa + \phi_{i,j+2} + 4\phi_{i,j+1} - 5\phi_{i,j})/(4\delta_x^2) \tag{26}$$

where in evaluating $\partial_{yy} \phi|_{i,j}$ the following biased difference schemes

$$\partial_{yy} \phi|_{i,j} \approx (-3\partial_y \phi|_{i,j} + 4\partial_y \phi|_{i,j+1} - \partial_y \phi|_{i,j+2})/(2\delta_x) \tag{27}$$

$$\partial_y \phi|_{i,j+2} \approx (3\phi_{i,j+2} - 4\phi_{i,j+1} + \phi_{i,j})/(2\delta_x) \tag{28}$$

and the central difference scheme

$$\partial_y \phi|_{i,j+1} \approx (\phi_{i,j+2} - \phi_{i,j})/(2\delta_x) \tag{29}$$

have been used. On the upper wall and even in three dimensions, similar formulas can be derived but for brevity they are not presented here. Using these formulas, $\nabla\phi$ and $\nabla^2\phi$ required in the lattice Boltzmann equations are easily obtained on the boundary.

4. RESULTS AND DISCUSSION

In this section, LBM simulations of semicircular (in 2D) or hemispherical (in 3D) droplets on a flat wall with given (variable) wetting properties are presented to illustrate the effects of mobility on the evolution routes as well as the final states of such two-phase fluid systems. It is noted that the values for mobility are given in terms of $\tilde{M}$. In what follows, all the numerical results are shown in the lattice units. Using the following relationships, the lattice quantities can be easily converted to the physical quantities. Suppose that $l_{\text{physical}}, u_{\text{physical}}, t_{\text{physical}}$ are the length, velocity and time in the physical system, and $l_{\text{LBM}}, u_{\text{LBM}}, t_{\text{LBM}}$ are the length, velocity and time in the lattice Boltzmann frame. Correspondingly, the reference length, velocity and time in the two systems are, respectively, $L^{\text{ref}}_{\text{physical}}, U^{\text{ref}}_{\text{physical}}, t^{\text{ref}}_{\text{physical}}$ and $L^{\text{ref}}_{\text{LBM}}, U^{\text{ref}}_{\text{LBM}}, t^{\text{ref}}_{\text{LBM}}$. Usually, the reference time can be calculated by the reference length and velocity using the following relationships:

$$t^{\text{ref}}_{\text{physical}} = \frac{L^{\text{ref}}_{\text{physical}}}{U^{\text{ref}}_{\text{physical}}} \tag{30}$$

$$t^{\text{ref}}_{\text{LBM}} = \frac{L^{\text{ref}}_{\text{LBM}}}{U^{\text{ref}}_{\text{LBM}}} \tag{31}$$

DOI: 10.1002/fld

Note that the reference quantities may be different from the characteristic quantities. They must be taken in both systems at the same location and status. The basic principle for the conversion is that the non-dimensional quantities in the two systems must be the same, that is,

$$\frac{l_{\text{physical}}}{L^{\text{ref}}_{\text{physical}}} = \frac{l_{\text{LBM}}}{L^{\text{ref}}_{\text{LBM}}} \tag{32}$$

$$\frac{u_{\text{physical}}}{U^{\text{ref}}_{\text{physical}}} = \frac{u_{\text{LBM}}}{U^{\text{ref}}_{\text{LBM}}} \tag{33}$$

$$\frac{t_{\text{physical}}}{t^{\text{ref}}_{\text{physical}}} = \frac{t_{\text{LBM}}}{t^{\text{ref}}_{\text{LBM}}} \tag{34}$$

For a given physical problem, one can easily decide the reference length and velocity. In the LBM calculation, the lattice mesh spacing δ_x is usually taken as 1 (also used in the present work). Suppose that the non-dimensional mesh spacing in the physical system is Δx, then the reference length in the lattice Boltzmann frame is $L^{\text{ref}}_{\text{LBM}} = 1/\Delta x$. Hence, all the length units in LBM results including the interface width W must multiply Δx when they are converted into those in the physical system. Owing to the incompressible limit, the reference velocity in the LBM computation must be less than 0.3. For the problem considered (droplet), we can take the maximum vertical velocity of the droplet as the reference velocity. From the LBM results, $U^{\text{ref}}_{\text{LBM}}$ (maximum vertical velocity of the droplet) is about 0.004 in the present work. If the maximum vertical velocity of the droplet in the physical system is known as $U^{\text{ref}}_{\text{physical}}$, then the physical velocity u_{physical} can be easily calculated by Equation (33). With $L^{\text{ref}}_{\text{LBM}}$ and $U^{\text{ref}}_{\text{LBM}}$, we can simply get $t^{\text{ref}}_{\text{LBM}}$ by using Equation (31). Therefore, we can compute the non-dimensional time as $t_{\text{LBM}}/t^{\text{ref}}_{\text{LBM}}$, which can be used to calculate the time in the physical system since it is the same in any system. The conversion of other variables can be done in the same way as their non-dimensional values are the same in any system.

4.1. Droplet dewetting on a flat wall

In this subsection, we present some results about droplet dewetting on a flat wall with spatially homogeneous wettability. The lower wall is originally neutral wetting ($\tilde{\omega} = 0, \theta = 90^\circ$) and the droplet takes a semicircular (or hemispherical) shape when in equilibrium.

4.1.1. 2D study. At first, we consider a 2D problem. The domain size is taken as 100×50 for all cases. The initial droplet radius is set to be 20 and the droplet center is at $(x_d, y_d) = (50, 0.5)$. At the beginning, the lower wall is abruptly changed to be very lyophobic characterized by a large static CA ($\tilde{\omega} = -0.5865, \theta \approx 150^\circ$, which results in an initial CA difference $\Delta\theta = 150^\circ - 90^\circ = 60^\circ$). Such a change is similar to the situation in the electrowetting experiments [17] when a voltage is suddenly applied. In fact, researchers have invented some intriguing methods to modify the wall wettability such as shedding ultraviolet light or blue light onto a photoresponsive surface [18]. Another interesting way to achieve such a setup is given in [19] which may deserve certain attention here due to the similarity between their observations and part of the simulation results that will be shown below. In [19] initially there were some triangular gold nanostructures on graphite; then, laser was applied to melt these structures which turned into liquid and the molten nanodroplets

DOI: 10.1002/fld

experienced a dewetting process. When they maintained the liquid form for sufficiently long time, such nanodroplets might jump off the surface.

Before the simulation results are shown, several quantities are firstly defined, which reflect some characteristics of this problem. The first two are the average center y-coordinate ($\bar{y}_{\text{drop}}$) and the average velocity ($\bar{v}_{\text{drop}}$) of the droplet, calculated by

$$\bar{y}_{\text{drop}} = \sum_{i,j} y_{i.,j} N(\phi_{i,j}) \Big/ \sum_{i,j} N(\phi_{i,j}) \tag{35a}$$

$$\bar{v}_{\text{drop}} = \sum_{i,j} v_{i.,j} N(\phi_{i,j}) \Big/ \sum_{i,j} N(\phi_{i,j}) \tag{35b}$$

where the function $N(\phi)$ is defined as

$$N(\phi) = \begin{cases} 1 & (\phi > 0) \\ 0 & (\phi \leqslant 0) \end{cases} \tag{36}$$

Besides them, we also look at the total kinetic energy of the droplet and that of the whole field calculated by

$$KE_{\text{drop}} = \sum_{i,j} (1/2) |\mathbf{u}_{i,j}|^2 N(\phi_{i,j}) \tag{37a}$$

$$KE_{\text{total}} = \sum_{i,j} (1/2) |\mathbf{u}_{i,j}|^2 \tag{37b}$$

To better appreciate the evolutions of the small regions around the three-phase point, the dynamic CA θ_{dyn} is extracted from the phase field. The calculation follows the following formula [20]:

$$\theta_{\text{dyn}} = (180/\pi) \arccos[-(\mathbf{n} \cdot \nabla\phi)/|\nabla\phi|] \tag{38}$$

Two notes are in order for Equation (38). Firstly, the interface spans a few grid points; thus, we find several values for θ_{dyn} across the interfacial region, but we just take the maximum one, which is the most accurate. Secondly, when the droplet is away from the surface after dewetting, we simply set θ_{dyn} to be 180° for convenience.

In addition, half of the distance between the two three-phase points on the lower wall, denoted as R_x, is recorded. From R_x the contact line velocity V_{CL} is calculated by simple derivation with respect to time. For instance, the contact line velocity at time step t^n, V_{CL}^n, is obtained as

$$V_{\text{CL}}^n = (R_x^n - R_x^{n-1})/\delta_t \tag{39}$$

where R_x^n (R_x^{n-1}) is the value recorded at t^n (t^{n-1}).

Table I. Common parameters for simulations.

Parameters	Value
Surface tension σ	0.005
Interface thickness W	3
Kinematic viscosity v	0.005
Upper wall wettability (CA) θ_u	90°

DOI: 10.1002/fld

Some other parameters for simulations are listed in Table I. Note that these parameters are in lattice units. For a general case, the kinematic viscosity v and the surface tension σ should be calculated from the given Reynolds number Re and Capillary number Ca. However, for the present work, the characteristic velocity (maximum vertical velocity of the droplet) is not known before the simulation. Thus, v and σ are specified, which can be used to compute Re and Ca once the maximum vertical velocity of the droplet is obtained from the simulation. Figure 2 compares two series of snapshots of the droplet shapes every 10^3 steps for $\tilde{M}=5$ and 15. For both cases, when the wettability is abruptly changed, the droplet begins to contract, approaching the equilibrium configuration. After some time the droplet shrinks to such a shape that corresponds to a CA larger than the static equilibrium one. Then, two different outcomes occur: if the mobility is small ($\tilde{M}=5$), the droplet spreads after this overshoot, and thereafter experiences some oscillations on the wall until it obtains the shape of static equilibrium; in contrast, if the mobility is large enough ($\tilde{M}=15$), the droplet jumps off the wall, oscillates as well but completely inside the ambient fluid and finally takes a circular shape. This resembles the experimental findings in [19] to a large extent.

The dynamic CAs at the time steps shown in Figure 2 are provided in Figure 3. In all the three cases, the dynamic CA starts from about 90° in accordance with the initial condition. In the early stage, there are rather small differences between them: the dynamic CA just increases quickly to approach the equilibrium CA; after it approaches to the equilibrium one, it decreases slowly and then increases again. Significant differences occur between $t=3\times10^3$ and 4×10^3, after which the CA in the case with the largest mobility becomes 180°, whereas for the other two it experiences some oscillations before returning to the equilibrium state.

In Figure 4, the evolutions of the droplet center and velocity in the vertical direction are given for $\tilde{M}=5$, 10 and 15. In agreement with the direct observations, when the mobility is small ($\tilde{M}=5, 10$) $\bar{y}_{\text{drop}}$ shows some oscillations before it finally reaches a constant value (~13) corresponding to the equilibrium configuration; but when $\tilde{M}=15$, $\bar{y}_{\text{drop}}$ almost keeps increasing until it becomes constant (~24) when all the kinetic energy has been dissipated. Based on the maximum droplet velocity ($\bar{v}^{\max}_{\text{drop}}\sim0.004$), the Reynolds number and the capillary number are estimated to be $Re=\bar{v}^{\max}_{\text{drop}}R_d/v\sim16$ and $Ca=(\rho_c v)\bar{v}^{\max}_{\text{drop}}/\sigma\sim0.004$, respectively. In addition, the Cahn number is $Ch=W/R_d=0.15$. Here the characteristic length is chosen as the drop radius. If it is chosen as the domain size, then the Cahn number will be 0.03. The Peclet number, $Pe=\bar{v}^{\max}_{\text{drop}}R_d^2/[(1/2)\tilde{M}\delta_t]\sigma$, is within the range of $42.7\leqslant Pe\leqslant128$ (dependent of M).

Figure 5 compares the evolution of the kinetic energy of the droplet as well as the whole flow field under the three mobilities. From Figure 5 it is seen that for all cases, the kinetic energy increases quickly at the initial stage, reaches a maximum and then decays quickly. This corresponds to the transformation of the potential energy (due to the initial non-equilibrium configuration) of the concentration field into kinetic energy of the flow field, and then vice versa. The larger the mobility is, the higher the extreme kinetic energy can reach. This may suggest that the mobility facilitates the release of the potential energy at the beginning, possibly due to the increase in contact line velocity with increasing mobility. After this stage, the kinetic energy decays due to dissipating effects. It is interesting to note that, contrary to the maximum in the initial stage, the next-to-maximum of the kinetic energy decreases when the mobility increases. This is probably due to the fact that the dissipation by molecular diffusion increases with larger mobility and it becomes more significant in the later stages. Finally, it is observed that the droplet experiences more oscillations if it is completely immersed in the ambient fluid than when it still stays attached on the wall. This is reasonable because the wall tends to have larger retardation on it.

DOI: 10.1002/fld

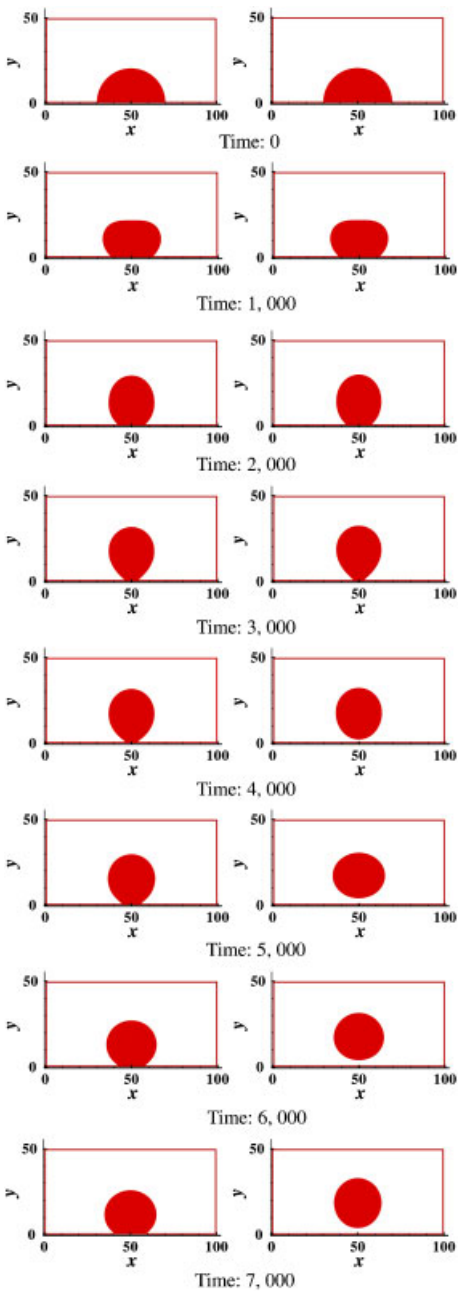

Figure 2. Snapshots of droplet shapes every 1000 steps after the wall wettability is suddenly switched from neutral wetting to very lyophobic (left: $\tilde{M}=5$; right: $\tilde{M}=15$).

DOI: 10.1002/fld

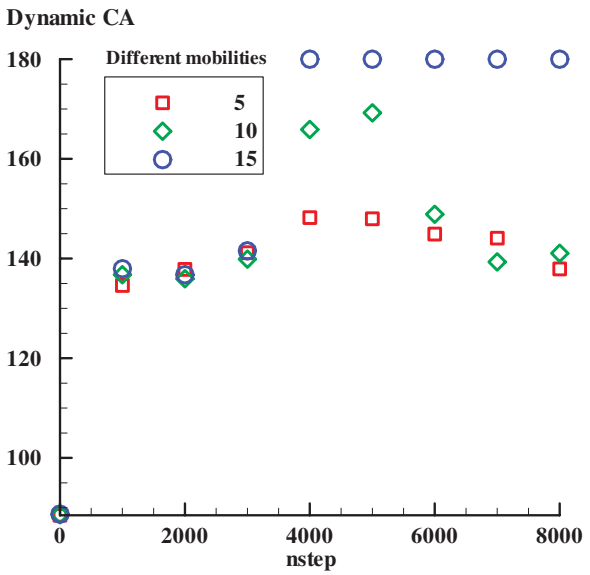

Figure 3. Evolution of the dynamic CA at time intervals shown in Figure 2.

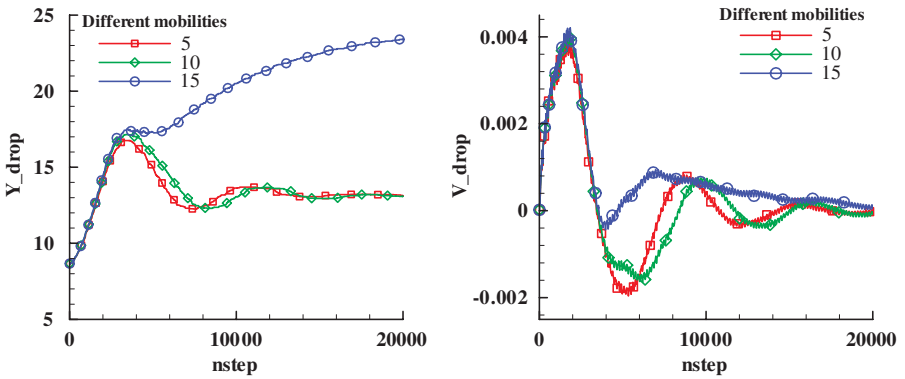

Figure 4. Evolution of the average center y-coordinate ($\bar{y}_{\text{drop}}$) and the average velocity ($\bar{v}_{\text{drop}}$) of the droplet under different mobilities.

Figure 6 shows the evolutions of R_x on the wall from $t=0$ to 2×10^4 for the three cases. This figure may illustrate different evolutions of the droplet in a clearer way. It is found that R_x first has some oscillations for $\tilde{M}=5$ and 10 and finally approaches a finite value (~ 8) corresponding to the configuration with static CA; when $\tilde{M}=15$, R_x keeps decreasing and becomes zero at about $t=3.6\times10^3$, which indicates that the droplet completely 'jumps up'.

As mentioned earlier, the contact line velocity, V_{CL}, can be obtained by differentiating R_x with respect to time. Its evolution is plotted in Figure 7. Similar to the dynamic CA, the evolutions of V_{CL} in the early stage for different cases are rather close. But there are some differences at the

DOI: 10.1002/fld

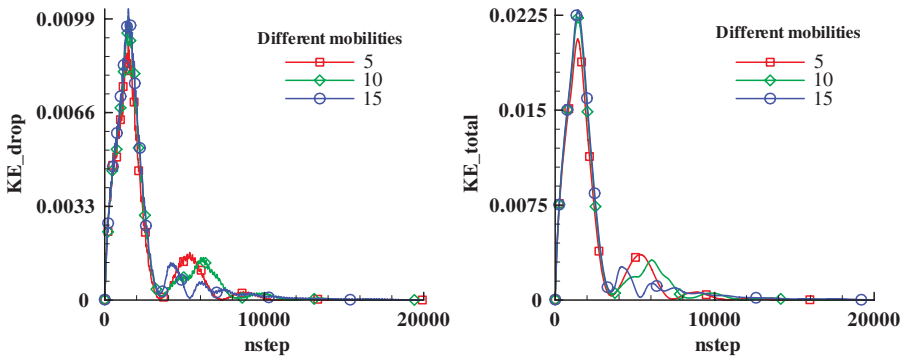

Figure 5. Evolution of the kinetic energy of the droplet (KE_{drop}) and the whole flow field (KE_{total}) under different mobilities.

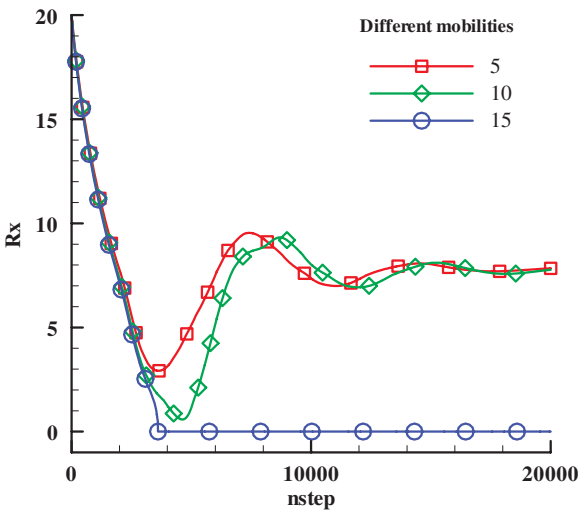

Figure 6. Evolution of R_x on the wall for different mobilities.

beginning: the magnitudes of V_{CL} at $t=10$ for $\tilde{M}=5$, 10 and 15 are 0.01103, 0.01771 and 0.02264, respectively. For the case of $\tilde{M}=15$, $|V_{CL}|$ displays a surge before the droplet gets away from the wall (at about $t=3.6\times10^3$). The reason may be related to the singularity that occurs at this specific stage. After that, $|V_{CL}|$ is not well defined; thus, in Figure 7 only the period during which the droplet was attached to the wall is shown. For the other two cases ($\tilde{M}=5$ and 10), some oscillations and then a tendency to reach equilibrium are found, as expected from the evolution of R_x.

To obtain the critical value for mobility, many simulations have been carried out. Figure 8 shows the evolutions of R_x from $t=3\times10^3$ to 6×10^3 for a series of mobility across the critical value. From this figure, it is seen that the critical $\tilde{M}$ lies in between 10 and 10.1 (by a rough estimation, one may take $\tilde{M}_{cr}\approx10.05$).

DOI: 10.1002/fld

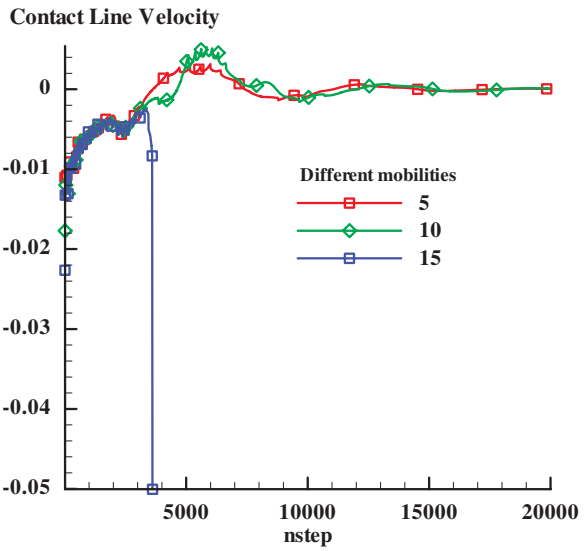

Figure 7. Evolution of the contact line velocity for different mobilities.

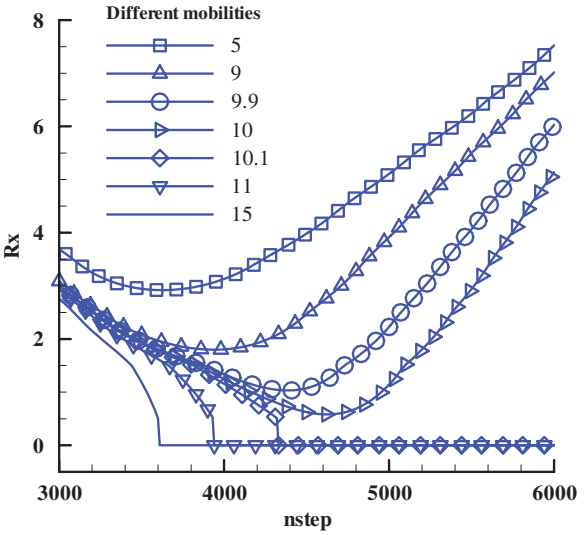

Figure 8. Bifurcation diagram of the evolution of R_x under different mobilities.

In addition, from this set of numerical experiments, the initial contact line velocity (at $t = 10$) as a function of the mobility has been extracted (see Figure 9). It is observed that the relation may be roughly described by a linear function ($V_{\mathrm{CL}} \propto \tilde{M}$). However, it should be noted that this relation may hold only within a certain range of $\tilde{M}$ and at the early stage of dewetting plus under

DOI: 10.1002/fld

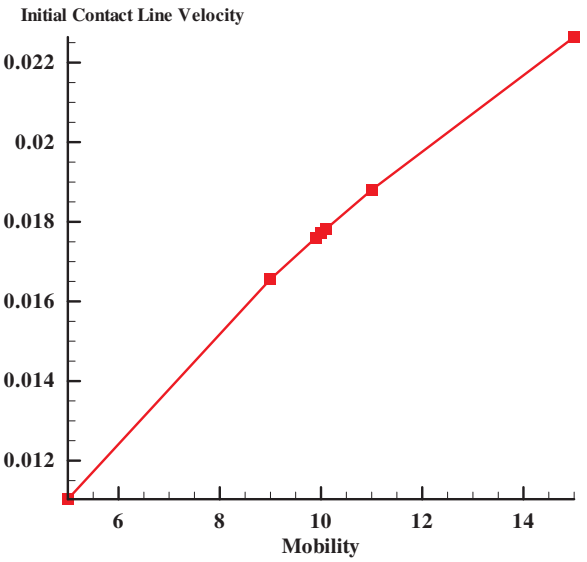

Figure 9. Variation of the initial contact line velocity with the mobility.

the capillary number regime investigated. At late stages, it may not hold because of the change in the droplet shape and other non-linear factors.

Finally, it would be interesting to compare the above results with the work of [21], in which the dewetting process of a thin liquid film was studied both experimentally and by using a lubrication model with a slip condition. The radius of the hole and the rim profile were mainly investigated. It was found that two different lubrication models can result from slip lengths different by order of magnitude. That is quite similar to the present findings though here the dewetting of semicircular droplets is investigated.

4.1.2. Effects of initial CA difference and surface tension on critical mobility. In the droplet dewetting process, the initial CA difference $\Delta\theta$ and the surface tension σ are certainly two important factors. The variation of the critical mobility $\tilde{M}_{cr}$ with $\Delta\theta$ (at a fixed σ), as well as its variation with σ (with $\Delta\theta$ fixed), is worth studying. A series of simulations varying θ while fixing σ (and vice versa) were carried out to find $\tilde{M}_{cr}$ to the accuracy of 0.1 and the average value was chosen as the critical one (similar to the above case in which $\tilde{M}_{cr} \approx 10.05$).

Figure 10 shows the variation of $\tilde{M}_{cr}$ with $\Delta\theta$ (while the surface tension is fixed as $\sigma = 0.005$). The results are from 11 series of tests with the lower wall CA varying from 150° to 160° (at 1° interval). Note that the $\tilde{M}_{cr}$ axis is plotted using the log scale. It is seen that as the CA difference increases, $\tilde{M}_{cr}$ decreases, which means that the droplet jumps off the surface easier. This can be understood from the direct physical analysis. Large $\Delta\theta$ is equivalent to large initial potential energy or driving force; thus, bifurcation may still happen even when the slip on the wall (related to the mobility) is weak under such conditions. Another trend is that when $\Delta\theta$ decreases, $\tilde{M}_{cr}$ seems to increase faster and faster (i.e. the rate of increase becomes larger as well). In Figure 10 $\tilde{M}_{cr}$ is in the log scale and the data distribution seems to be close to one straight line (the dashed line drawn for reference) for relatively small $\Delta\theta$ (roughly $\Delta\theta < 65°$), and it is close to another straight line

DOI: 10.1002/fld

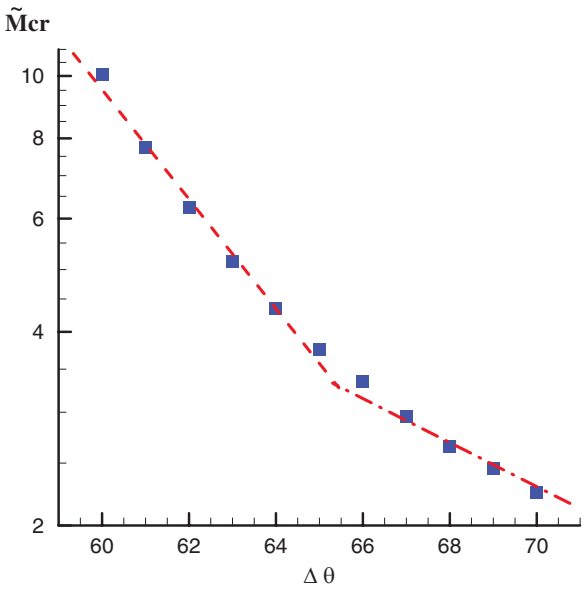

Figure 10. Variation of the critical mobility with the initial CA difference (note that the dashed and the dashed-dotted lines are drawn for reference).

(e.g. the dashed-dotted line) for relatively large $\Delta\theta$ (roughly $\Delta\theta > 65°$). For $\Delta\theta < 65°$ one may deduce that $\tilde{M}_{\mathrm{cr}}$ may increase exponentially as $\Delta\theta$ decreases. In the simulations with $\Delta\theta = 55°$ ($\theta = 145°$) the bifurcation could no longer be observed. No matter how the mobility was varied, the droplet always stayed on the lower wall after the dewetting process. This indicates that at this CA, $\tilde{M}_{\mathrm{cr}}$ (if any) already exceeds the one that would guarantee numerical stability. At the other end, for $\Delta\theta > 65°$, $\tilde{M}_{\mathrm{cr}}$ seems to decrease at a slower rate as $\Delta\theta$ increases.

The effect of the surface tension σ on $\tilde{M}_{\mathrm{cr}}$ can be found in Figure 11. Five series of simulations with σ from 0.003 to 0.005 (at an interval of 0.0005) were performed at $\Delta\theta = 65°$ (i.e. θ fixed to be 155°). Both $\tilde{M}_{\mathrm{cr}}$ and σ axes are plotted in log scale. It is found that the points are almost on a straight line (the dashed line). This suggests that the two may be related by $\tilde{M}_{\mathrm{cr}} = C_2 \sigma^{-C_1}$, where C_1 and C_2 are positive constants. It is obvious that $\tilde{M}_{\mathrm{cr}}$ decreases when σ increases. From the trend, it is possible that $\tilde{M}_{\mathrm{cr}}$ could go beyond the value that allows numerical stability as σ further decreases (to be far below 0.003); for very large σ (to be much larger than 0.005), the droplet might jump away from the wall for any (numerically allowed) value of $\tilde{M}$ (just like the situation for the $\tilde{M}_{\mathrm{cr}}$–$\Delta\theta$ relation). However, the investigations of the two extremes are not within the scope of the present work. In addition, the $\tilde{M}_{\mathrm{cr}}$–σ relation deduced from Figure 11 may not hold when $\Delta\theta$ varies. What it will be like as $\Delta\theta$ changes is left for future study.

4.1.3. Some 3D investigations. In addition to the 2D study, a few 3D dewetting simulations, which are supposedly to be closer to the real situations, have also been performed. The domain size is $90 \times 90 \times 50$, the initial droplet radius is set to be $R_d = 15$ and the droplet center is at $(x_d, y_d, z_d) = (45, 45, 0.5)$. The viscosity v, the interface width W and other parameters remain the same as in the 2D study except that the surface tension is now smaller ($\sigma = 0.002$). Similar to the

DOI: 10.1002/fld

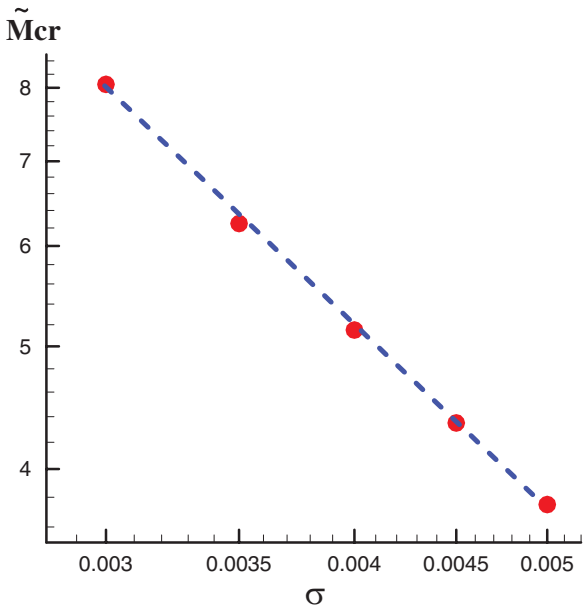

Figure 11. Variation of the critical mobility with the surface tension (note that the dashed line is drawn for reference).

2D case, periodic boundary condition is implemented at all boundaries. Two values for the lower wall CA (145° and 150°) were tested. In both cases, bifurcations depending on the mobility were observed. For a brief capture, the final states for the case of $\theta = 145°$ with the mobility being 4.5 and 5 are shown in Figure 12. In Figure 12(a), the droplet stays on the wall, whereas it jumps off the surface in Figure 12(b). The bifurcation diagrams in terms of the evolution of R_x (similar to the 2D definition, but now taken in the central x–z plane) are given in Figure 13. For the 3D case, we tried to find only the critical mobility $\tilde{M}_{\text{cr}}$ to the accuracy of 0.5. Using an estimation based on the average of the two mobilities across the critical one, $\tilde{M}_{\text{cr}}$ would be 4.75 and 2.25 for $\theta = 145°$ and 150°, respectively. For the four cases ($\theta = 145° : \tilde{M} = 4.5, 5$; $\theta = 150° : \tilde{M} = 2, 2.5$), the recorded maximum droplet velocities in the z-direction ($\bar{w}_{\text{drop}}^{\max}$) are in the range from 0.0032 to 0.0034 (the mid-value 0.0033 is taken for convenience). Based on $\bar{w}_{\text{drop}}^{\max} \sim 0.0033$, the Reynolds number and the capillary number are roughly given by $Re = \bar{w}_{\text{drop}}^{\max} R_d / \nu \sim 9.9$ and $Ca = (\rho_c \nu) \bar{w}_{\text{drop}}^{\max} / \sigma \sim 0.00825$, respectively. In addition, the Cahn number is $Ch = W/R_d = 0.2$, and the Peclet numbers, $Pe = \bar{w}_{\text{drop}}^{\max} R_d^2 / [(1/2)\tilde{M}\delta_t]\sigma$, are 371.25, 297, 165 and 148.5, respectively, for $\tilde{M} = 2, 2.5, 4.5$ and 5. By comparing Figure 13 with Figure 8, one can see clearly that the 3D results do confirm the finding in the 2D study. That is, there is a critical mobility for bifurcation with a given CA.

4.2. Droplets on a flat wall with chemical heterogeneity

Next we present some results about the mobility effect on 3D droplets on a flat wall with chemical heterogeneity. The computations were done in a domain of $0 \leqslant x \leqslant 50, 0 \leqslant y \leqslant 50, 0 \leqslant z \leqslant 25$ confined between two parallel walls at $z = 0$ and 25. On the other four sides, periodic boundary conditions were used. Hence in equivalence, we simulated a series of droplets and the neighboring droplets

DOI: 10.1002/fld

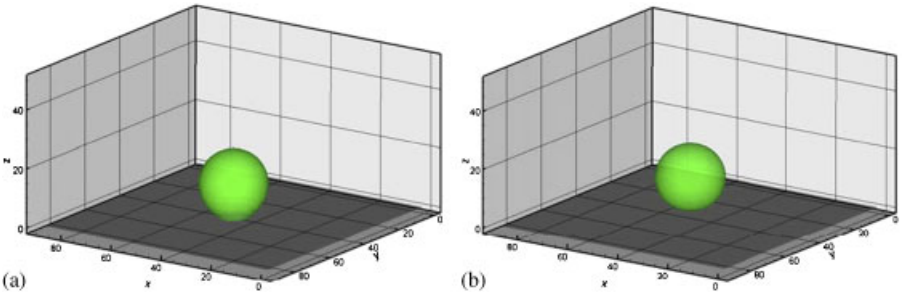

Figure 12. Snapshots of the droplet at the end of simulation (time: 10 000) for $\theta = 145°$: (a) mobility $\tilde{M} = 4.5$ and (b) mobility $\tilde{M} = 5$.

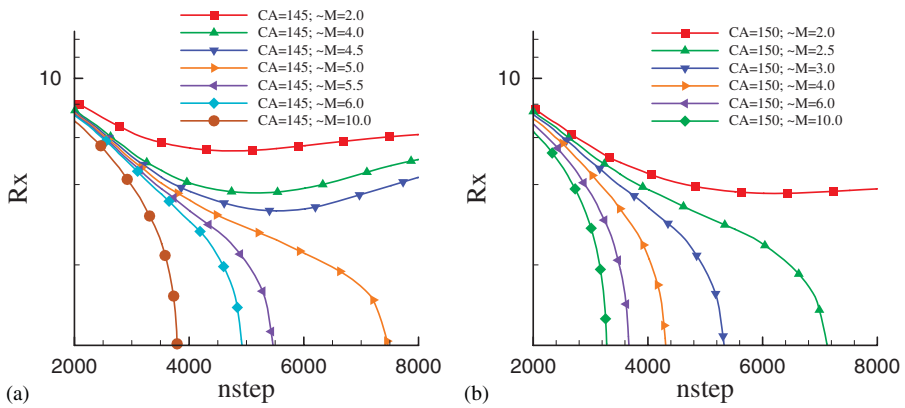

Figure 13. Bifurcation diagram of the evolution of R_x under different mobilities for a 3D droplet: (a) lower wall CA 145° and (b) lower wall CA 150°.

may coalescence with each other under certain conditions. Similar to the previous cases, the initial conditions are given for the walls being neutral wetting and the droplets take hemispherical shape in equilibrium. The droplet radius is $R_d = 16.5$ and the droplet center is at $(x_d, y_d, z_d) = (25, 25, 0)$. The wall at $z = 25$ is always kept neutral wetting. At the initial stage on the wall at $z = 0$, a narrow lyophobic ($\tilde{\omega} = -0.432, \theta \approx 130°$) stripe of width 6 is suddenly created near the center line of $x = 25$ (with slight asymmetry: 0.5 toward left) and all other parts are suddenly made lyophilic ($\tilde{\omega} = 0.335, \theta \approx 60°$) by some means (see Figure 14; note that to better illustrate the situation the right half $50 \leqslant x \leqslant 100, 0 \leqslant y \leqslant 50$, identical to the left, has been added). Some other parameters for simulations are listed in Table II. For this problem, we define an average droplet velocity magnitude by

$$|\mathbf{u}|_d = \sqrt{2 \sum_{i,j,k} (1/2)|\mathbf{u}_{i,j,k}|^2 N(\phi_{i,j,k}) \Big/ \sum_{i,j,k} N(\phi_{i,j,k})} \tag{40}$$

where the function $N(\phi)$ is defined in Equation (36).

DOI: 10.1002/fld

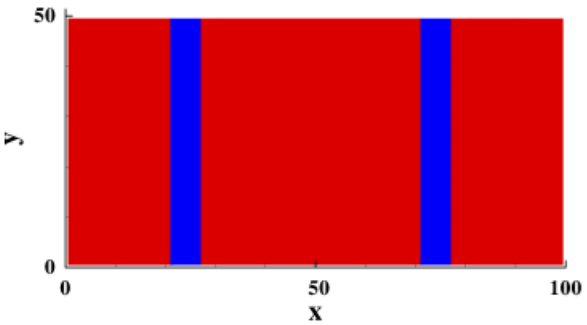

Figure 14. Wettability distribution on the wall at $z=0$ (slim stripe: lyophobic; other parts: lyophilic).

Table II. Common parameters for simulations.

Parameters	Value
Surface tension σ	0.001
Interface thickness W	3
Kinematic viscosity v	0.005

The evolution of this system is monitored every 10^3 steps. Figure 15 compares the snapshots of the system evolutions for $\tilde{M}=2$ and 20. Note that the data for the right half ($50\leqslant x\leqslant 100, 0\leqslant y\leqslant 50, 0\leqslant z\leqslant 25$) are duplicated from that for the left half in order to illustrate the evolution more clearly. It is easily seen that the fundamental differences result from the change in mobility. Because the two cases evolved with a different characteristic time, the snapshots were taken every 10^4 steps for $\tilde{M}=2$, whereas the interval was 4×10^3 for $\tilde{M}=20$. The evolutions of the average droplet $|\mathbf{u}|_d$ (as defined by Equation (40)) are shown in Figure 16. The observed maximum values of the droplet velocity, $|\mathbf{u}|^{\max}_{\text{drop}}$, were 0.0017 and 0.0018 for $\tilde{M}=2$ and 20, respectively. We may take their average, 0.00175, to roughly estimate the dimensionless numbers as $Re=|\mathbf{u}|^{\max}_{\text{drop}}R_d/v=5.775$, $Ca=(\rho_c v)|\mathbf{u}|^{\max}_{\text{drop}}/\sigma=0.00875$, $Ch=W/R_d=0.18$ and $Pe=|\mathbf{u}|^{\max}_{\text{drop}}R_d^2/[(1/2)\tilde{M}\delta_t]\sigma=476.4$ for $\tilde{M}=2$ and 47.64 for $\tilde{M}=20$.

For both cases, the droplets are driven by the chemical heterogeneities toward the equilibrium configurations that minimize the total energy of the system. Probably due to the slight asymmetry in the position of the lyophobic stripe the droplets tend to move toward right; thus for each droplet the right tip is an advancing point and the left, receding. When the mobility is small, the droplet moves much slower (smaller contact line velocity). Note that both the advancing and receding speeds are small. But the advancing point of the left droplet moves slower enough (relative to the receding velocity of the right droplet) and it is not able to catch up and coalesce with the right one; the droplets just experience some contractions when moving across the lyophobic islands and finally stay on the lyophilic lands. If the mobility becomes much larger, the contact line velocities of both the advancing and receding points increase. It seems that the increment in the advancing speed of the left droplet is more significant than that of the receding one of the right droplet. As a result, the left catches up with the right and merges with it. Eventually the all-connected large drop was again broken into small droplets staying on the lyophilic parts separated by the

DOI: 10.1002/fld

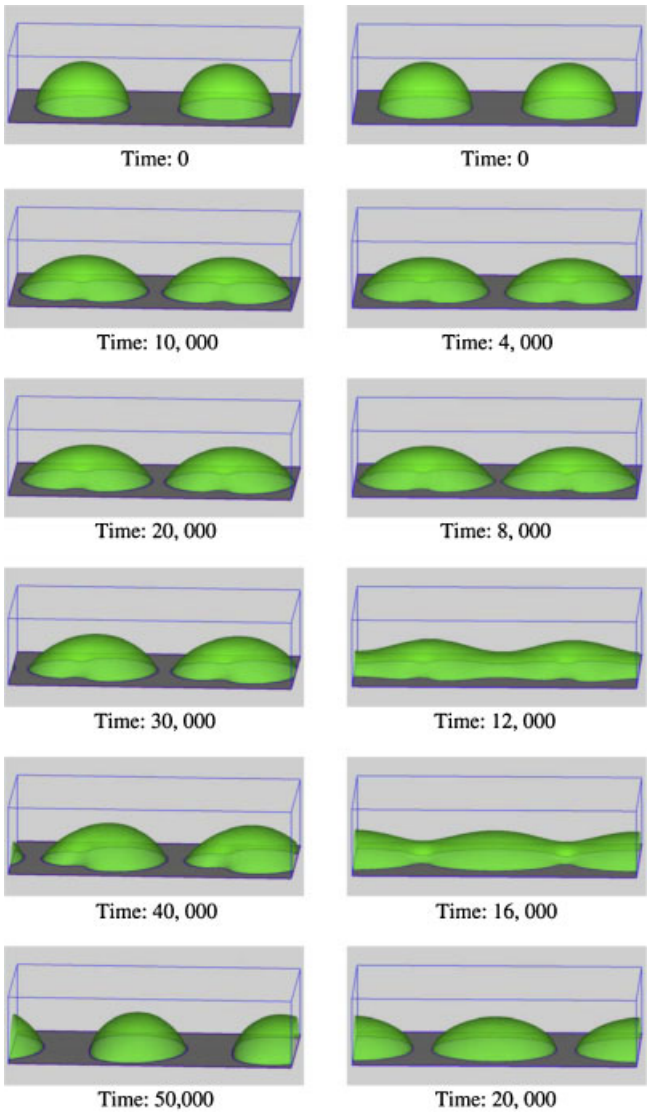

Figure 15. Snapshots of droplet shapes for $\tilde{M}=2$ (every 10^4 steps; left column) and for $\tilde{M}=20$ (every 4×10^3 steps; right column) on chemically heterogeneous walls.

lyophobic islands. It is noted that the two different processes are reflected in Figure 16 as well. When the droplet was simply driven to the lyophilic part without being split $(\tilde{M}=2)|\mathbf{u}|_d$ had only two peaks; but when the droplet experiences the merging-and-splitting process $(\tilde{M}=20)|\mathbf{u}|_d$ showed three peaks and decayed to zero much faster. Obviously, for this problem there should also be some critical value of mobility that differentiates the two routes. However, it requires considerable simulation efforts to get this value for the 3D case and we leave it for future work.

DOI: 10.1002/fld

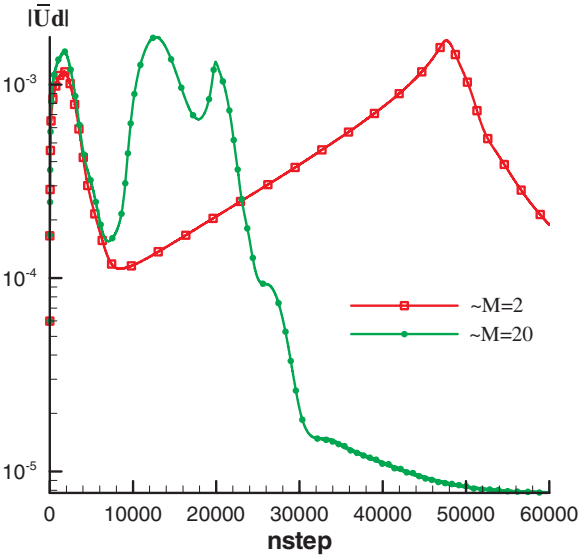

Figure 16. Evolution of the average droplet velocity $|\mathbf{u}|_d$ for $\tilde{M}=2$ and 20.

5. CONCLUSIONS

In this paper, we have studied the effects of mobility on chemically driven droplets by the lattice Boltzmann model. Through extensive numerical investigations of the droplet dewetting process (both 2D and 3D) and a preliminary study of droplets on heterogeneous surfaces, we have found that the mobility determines the slip velocity of the contact line and may critically decide the evolutions and final equilibrium states of such two-phase fluid systems. These investigations are expected to give some useful hints to future study in microfluidics involving droplet manipulations.

REFERENCES

1. Verberg R, Pooley CM, Yeomans JM, Balazs AC. Pattern formation in binary fluids confined between rough, chemically heterogeneous surfaces. *Physical Review Letters* 2004; **93**:184501.
2. Anderson DM, McFadden GB, Wheeler AA. Diffuse-interface methods in fluid mechanics. *Annual Review of Fluid Mechanics* 1998; **30**:139–165.
3. Jacqmin D. Calculation of two-phase Navier–Stokes flows using phase-field modeling. *Journal of Computational Physics* 1999; **155**:96–127.
4. Jacqmin D. Contact-line dynamics of a diffuse fluid interface. *Journal of Fluid Mechanics* 2000; **402**:57–88.
5. Chen H-Y, Jasnow D, Viñals J. Interface and contact line motion in a two phase fluid under shear flow. *Physical Review Letters* 2000; **85**:1686.
6. Kendon VM, Cates ME, Pagonabarraga I, Desplat J-C, Bladon P. Inertial effects in three-dimensional spinodal decomposition of a symmetric binary fluid mixture—a lattice Boltzmann study. *Journal of Fluid Mechanics* 2001; **440**:147–203.
7. Briant AJ, Yeomans JM. Lattice Boltzmann simulations of contact line motion. II. Binary fluids. *Physical Review E* 2004; **69**:031603.
8. Inamuro T, Ogata T, Tajima S, Konishi N. A lattice Boltzmann method for incompressible two-phase flows with large density differences. *Journal of Computational Physics* 2004; **198**:628–644.
9. Vladimirova N, Mauri R. Mixing of viscous liquid mixtures. *Chemical Engineering Science* 2004; **59**:2065–2069.

DOI: 10.1002/fld

10. Lamorgese AG, Mauri R. Mixing of macroscopically quiescent liquid mixtures. *Physics of Fluids* 2006; **18**:044107.
11. Khatavkar VV, Anderson PD, Meijer HEH. On scaling of diffuse-interface models. *Chemical Engineering Science* 2006; **61**:2364–2378.
12. Zheng HW, Shu C, Chew YT. A lattice Boltzmann model for multiphase flows with large density ratio. *Journal of Computational Physics* 2006; **218**:353–371.
13. Swift MR, Orlandini E, Osborn WR, Yeomans JM. Lattice Boltzmann simulations of liquid–gas and binary fluid systems. *Physical Review E* 1996; **54**:5041–5052.
14. Yuan P, Schaefer L. Equations of state in a lattice Boltzmann model. *Physics of Fluids* 2006; **18**:042101.
15. Chen S, Doolen GD. Lattice Boltzmann method for fluid flows. *Annual Review of Fluid Mechanics* 1998; **30**:329–364.
16. Briant AJ, Papatzacos P, Yeomans JM. Lattice Boltzmann simulations of contact line motion in a liquid–gas system. *Philosophical Transactions of the Royal Society of London*, *Series A* 2002; **360**:485–495.
17. Pollack MG, Fair RB, Shenderov AD. Electrowetting-based actuation of liquid droplets for microfluidic applications. *Applied Physics Letters* 2000; **77**:1725–1726.
18. Ichimura K, Oh S-K, Nakagawa M. Light-driven motion of liquids on a photoresponsive surface. *Science* 2000; **288**:1624–1626.
19. Habenicht A, Olapinski M, Burmeister F, Leiderer P, Boneberg J. Jumping nanodroplets. *Science* 2005; **309**: 2043–2045.
20. Ding H, Spelt PDM. Wetting condition in diffuse interface simulations of contact line motion. *Physical Review E* 2007; **75**:046708.
21. Fetzer R, Jacobs K, Munch A, Wagner B, Witelski TP. New slip regimes and the shape of dewetting thin liquid films. *Physical Review Letters* 2005; **95**:127801.

DOI: 10.1002/fld